Anisotropic elasticity of experimental colloidal Wigner crystals

Emily R. Russell, Frans Spaepen, and David A. Weitz

Phys. Rev. E **91**, 032310 — Published 17 March 2015

DOI: 10.1103/PhysRevE.91.032310

Anistropic elasticity of experimental colloidal Wigner crystals

Emily R. Russell,[1,*,†] Frans Spaepen,[2] and David A. Weitz[1,2]

[1] *Department of Physics and* [2] *School of Engineering and Applied Science, Harvard University, Cambridge, MA 02138*

February 19, 2015

Abstract

Colloidal particles interacting via a long-range repulsion can, in contrast to hard-sphere systems, exhibit crystalline ordering at low volume fraction. Here we experimentally investigate the structure and properties of such 'colloidal Wigner crystals'. We find a body-centered-cubic crystalline phase at volume fractions of $\phi \gtrsim 15\%$, which exhibits large fluctuations of individual particles from their average positions. We determine the three independent crystalline elastic constants, and find that these crystals are very compliant and highly anisotropic.

1 Introduction

Colloidal particles are often used to model atomic and molecular crystals, from the face-centered-cubic crystals formed by monodisperse hard-sphere or near-hard-sphere particles [1], to more complex crystal structures formed by heterogeneous mixtures of particles [2]. Colloidal crystals can also form at low volume fraction in a system with long-range repulsion [3, 4, 5, 6, 7, 8, 9, 10, 11, 12]. These crystals exhibit a body-centered-cubic structure, and are often called colloidal 'Wigner' crystals, in analogy to the minimum-energy configuration of electrons in a metal at low density and low temperature predicted by Eugene Wigner [13]. These crystals can be modeled by a screened-Coulomb or Yukawa potential [14, 15], and have been found to be extremely soft [5, 6, 7]. Yet only recently has the advent of confocal microscopy allowed direct visualization of individual particles in such crystals [10, 11, 12], which has raised many open questions regarding local fluctuations in these soft crystals.

Here we present a study of the detailed local structure and material properties of crystals formed by an experimental model system of charged colloids with a long-range repulsion. We demonstrate the formation of body-centered-cubic 'Wigner' crystals at volume fractions of $\phi \approx 15$ - 26%, and directly observe the local structure

[*] *Present address: Institute for Computational and Experimental Research in Mathematics, Brown University, Providence, RI 02912*

[†] *Emily_Russell@post.harvard.edu*

using confocal microscopy. We measure the fluctuations of particles from their positions in the crystalline lattice, and find that these fluctuations are unusually large relative to the conventional expectation of the Lindemann melting correlation. We calculate the thermally-activated local strains in the system, and find that these strains are correlated over short ranges of about two to three lattice constants. We determine the three independent crystalline elastic constants as a function of particle number density; these elastic constants exhibit a strong anisotropy, and we find that this anisotropy increases as we approach the melting volume fraction.

2 Experimental

Particles of poly-methyl-methacrylate (PMMA; 1.8μm diameter) coated with a brush of poly-hydroxystearic acid (PHSA) are suspended in a nonpolar solvent mixture of decahydronapthalene (decalin) and tetrachloroethylene (t.c.e.). The solvent ratio (roughly 55% decalin / 45% t.c.e. by volume) is chosen to match the mass density of the particles, and hence to minimize the effects of gravitational pressure. The particles are fluorescently dyed, and the refractive index of the solvent mixture is sufficiently close to that of the particles to permit imaging in three dimensions using confocal microscopy.

A long-range repulsion between particles is introduced by the addition of 10mM of the surfactant dioctyl sodium sulfosuccinate (commonly known as aerosol-OT or AOT). Above its critical micelle concenctration ($\approx$ 1mM), AOT forms micelles, of radius on the order of 1.5 nm; these micelles act as charge carriers in the solution, with roughly one in 10^5 micelles acquiring a single elementary charge [16]. They furthermore enable the dissociation of the PHSA groups on the surface of the particles, with the dissociated proton entering a micelle core, so that the particles acquire a negative charge and the interparticle interaction becomes repulsive [16]. The 10mM concentration was chosen to generate an optimum balance between highly charged particles (at large [AOT]) and long screening lengths (at low [AOT]), in order to achieve large interparticle spacings; at this AOT concentration, we anticipate a charge-carrier concentration on the order of 4 nM, and a Debye screening length of $\kappa^{-1} \approx 0.8$ - 1μm [16, 17, 18].

Samples are prepared at fixed volume fractions, and allowed to equilibrate over eight days before observations. We obtain three-dimensional image stacks using confocal microscopy, and employ standard analysis techniques [19, 20] to obtain precise locations over time of each particle in the imaging volume [21].

3 Results and discussion

Body-centered-cubic 'colloidal Wigner crystals' formed over a range of moderate particle number densities of $n = 0.054$ - $0.085(\mu\text{m})^{-3}$ (corresponding to volume fractions of $\phi \approx 15$ - 26%) [22]. Samples were polycrystalline,

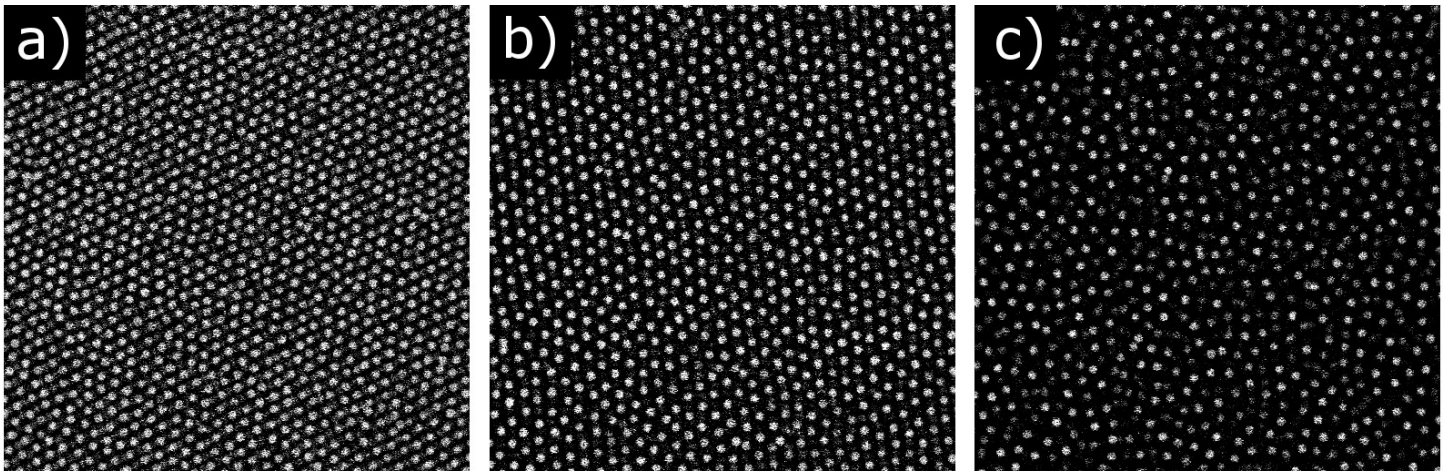

Figure 1: Confocal microscope images of repulsive charged-sphere systems at several number densities. a) (110) plane of a b.c.c. crystal at $n = 0.085(\mu\text{m})^{-3}$ ($\phi \approx 26\%$). b) (110) plane of a b.c.c. crystal at $n = 0.054(\mu\text{m})^{-3}$ ($\phi \approx 16\%$). c) Colloidal fluid at $n = 0.035(\mu\text{m})^{-3}$ ($\phi \approx 10\%$). All images are 82μm on a side.

with typical grain sizes between hundreds of micrometers and several millimeters; the number density within a single sample was not uniform, but varied by about $\Delta n \approx 0.002(\mu\text{m})^{-3}$ across different grains. The crystals always formed with a (110) plane parallel to the coverslip; examples of single planes are shown in Fig. 1a,b. This (110) plane has a stretched hexagonal structure and is the closest-packed plane of the b.c.c. crystal. The orientation indicates a boundary effect in the formation of the crystals, but we found that in most samples, the boundary effects did not extend to the fluctuations or material properties. The b.c.c. crystal gave way to a colloidal fluid at lower number densities of $n \lesssim 0.045(\mu\text{m})^{-3}$ (Fig. 1c).

Individual particles fluctuate significant distances from their positions in the average lattice. This is visible in single snapshots of the crystal (e.g. Fig. 1a,b), where both the average lattice and the deviations of particles from the average lattice are apparent. The dynamics of these fluctuations are also readibly visible from data collected over time, with particles moving on the timescale of seconds.

One measure of the degree of motion in the system is the mean-squared displacement (m.s.d.) of particles over a delay time Δt:

$$\text{m.s.d.}(\Delta t) = \left\langle \big(x(t+\Delta t) - x(t)\big)^2 \right\rangle - \left\langle \big(x(t+\Delta t) - x(t)\big) \right\rangle^2 \tag{1}$$

with the average taken over all particles and all starting times t. In particular, the m.s.d. at long delay times indicates whether the system behaves as a fluid or as a solid, and for a solid, indicates the time- and length-scales of the fluctuations of particles about their average positions. For a crystalline sample, we expect the m.s.d. to increase linearly with time at short times, as the particles diffuse within the potential wells due to interparticle interactions, and then to reach a plateau at long times, as particles are localized on the lattice, and in the absence of lattice defects, unable to diffuse freely. Several examples of the mean-squared displacements for crystalline

samples are shown in Fig. 2a; the experimental resolution of 2s is similar to the localization timescale, so that the short-time increase is barely captured, but the plateau region is clearly apparent. The value at which the *root*-mean-squared displacement (r.m.s.d.) plateaus, δr_t, can be considered as a 'localization lengthscale' of the fluctuations. In some samples, the m.s.d. increases again at later times, suggestive of particles slowly diffusing through the crystal; this could be the result of particles moving to different lattice sites, but our analysis is not conclusive.

The unitless *Lindemann parameter* δ_L gives the r.m.s.d. from the average position, $\delta r_{\bar{r}}$, as a proportion of the nearest-neighbor spacing a: $\delta_L \equiv \delta r_{\bar{r}}/a \approx \delta r_t/(\sqrt{2}a)$. This parameter is associated with the assumption of Lindemann, commonly reformulated to state that the value of this proportion at melting is a constant for monatomic solids; this assumption has been observed to be a good correlation for many elemental metals with cubic structures, with a critical value of $\delta_{L,c} \approx 0.07$ - 0.1, and is often interpreted as a melting criterion or law [23, 24]. In these experimental colloidal Wigner crystals, the Lindemann parameter appears to be nearly constant with number density over the range investigated (Fig. 2b), with perhaps a slight increase at the lowest number densities. At all number densities, it is significantly larger than 0.1.

An average lattice can be fit to all the particle positions. The lattice is constrained to have a b.c.c. structure, enforcing a single lengthscale and orthonormality of the cubic crystal axes. The lattice is then described by seven parameters: one lengthscale, for which we use the side length l of the cubic unit cell; three angles representing the rotation of the cubic lattice directions with respect to the imaging coordinates, expressed as a 3x3 orthonormal rotation matrix; and the three-component offset vector giving the translation of the lattice origin with respect to the origin of the imaging coordinates. These seven parameters are calculated independently at each timestep from the 3D locations of typically 1000-2000 particles in a single imaging volume.

The fit of the particle positions to a b.c.c. lattice is good. We examine the constraint that the three lengthscales of the crystalline lattice are equal by calculating the overall uniaxial strain of the system in each of the three cubic lattice directions. Taking the sample at $n = 0.054(\mu m)^{-3}$ as an example, we find a slight extension in the (lattice) X direction, and a slight compression in the (lattice) Z direction, but that the magnitude of the uniaxial strain in any dimension is less than 1%. Similarly, we examine the constraint that the crystalline cubic axes are normal by considering the overall shear of the system in each of the three cubic planes. We find slight shear strains in each component, but again less than 1%. Thus we are confident that our description of the system by an average b.c.c. lattice is valid. We further find that the definition of the average lattice is stable with time. The lattice parameters fluctuate with time, but the variations are small: the lattice cube side varies by less than 0.5%; the rotation angles by less than 1°; while the offset of the origin moves by less than 0.5μm. Finally, we verify that the

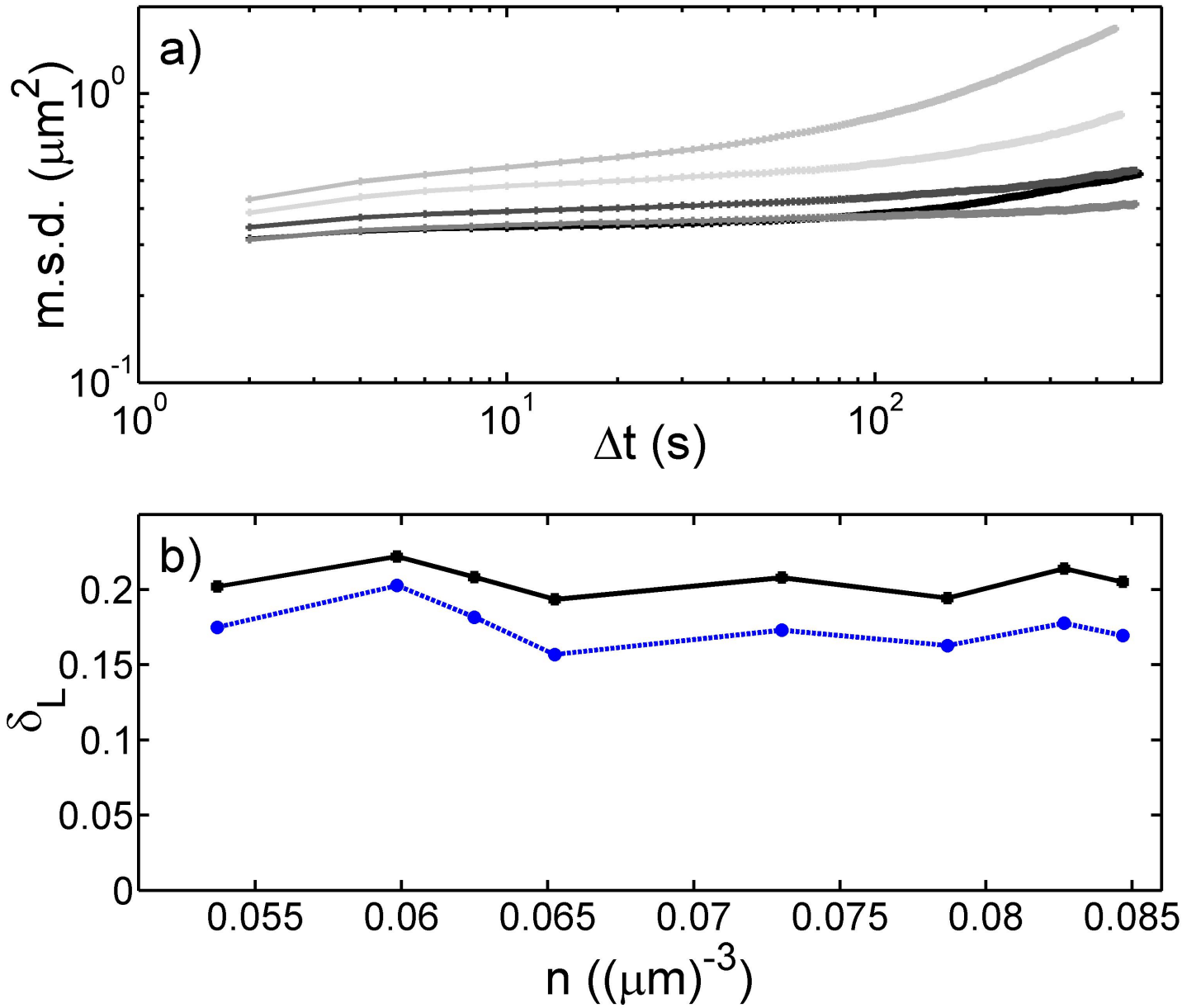

Figure 2: Scale of fluctuations of particles in experimental colloidal Wigner crystals. a) Total mean-squared displacements of particles with time for crystalline samples. Number density is indicated by shading: from dark to light, $n = 0.085, 0.073, 0.065, 0.060,$ and $0.054(\mu\text{m})^{-3}$. Note that the curves show a distinct plateau at intermediate times, indicating the localization of particles near the lattice positions. b) Lindemann parameter $\delta_L \equiv \delta r_{\bar{r}}/a$, calculated using the temporal mean-squared displacements ($\delta_L \equiv \delta r_t/(\sqrt{2}a)$, lower curve), and using displacements from the nearest average-lattice position ($\delta_L \equiv \delta r_l/a$, upper curve). Note that both measures give values larger than the conventional Lindemann correlation at the melting point, $\delta_{L,c} \approx 0.1$, and both are roughly constant with number density.

calculation of the average lattice does not change significantly if we use subsets of a 3D image to fit the lattice.

Using this average lattice, each particle can be identified with a nearest lattice position, and its displacement from that lattice position determined; the root-mean-squared average displacement from the lattice position, δr_l, provides a time-independent measure of the fluctuations in the crystal. This r.m.s.d. from the lattice position is then used to calculate another Lindemann parameter, $\delta_L = \delta r_l / a$, to be compared to the value calculated using the temporal r.m.s.d. (Fig. 2b). Curiously, these two measures of the mean-squared displacement give slightly different results. However, both calculations give large values of the Lindemann parameter, and little variation with number density.

Local deformation of the lattice is quantified by the local strains. We calculate these strains from the locations of a central particle and its crystallographic nearest- and next-nearest-neighbors (up to 15 particles in total), by finding the best affine deformation tensor from the particles' reference lattice positions to their measured positions, and taking the symmetric part as the strain tensor $\bar{\bar{\varepsilon}}$ (this method is originally due to Falk and Langer) [25, 26, 27]. Strains are expressed in the coordinates of the cubic axes of the lattice, and the strains are related to the tensor components by $e_{ii} = \varepsilon_{ii}$ for tensile strains, and $e_{ij} = \varepsilon_{ij} + \varepsilon_{ji} = 2 \cdot \varepsilon_{ij}$ for shear strains. A shear strain tensor component, ε_{xy}, is visualized for one sample in Fig. 3a. While small strains are most common, strains of up to $\approx 20\%$ are readily observed.

We use the thermal distributions of strains to calculate the elastic constants of the system [26, 27]. Creation of an average shear strain e over volume V requires energy $E = \frac{1}{2}\mu e^2 V$, where μ is the shear modulus, and for thermal excitations, we expect a Boltzmann distribution with $P(E) \propto \exp(-E/k_B T)$. Thus a linear fit to $\log P$ vs. $E/\mu k_B T = \frac{1}{2} e^2 V / k_B T$ yields the elastic constant μ as the negative of the slope. Here we use an averaging volume of a cube of side two lattice units, so that $V = (2l)^3$, and an averaging volume typically contains 16 particles.

Thermal distributions of different strain components are used to determine different elastic moduli. A cubic crystal is characterized by three independent elastic constants: c_{11}, c_{12}, and c_{44}. The shear modulus c_{44} is directly obtained from the distribution of shear strains $\{e_{xy}, e_{xz}, e_{yz}\}$ expressed relative to the cubic axes. The other elastic constants, c_{11} and c_{12}, are obtained indirectly from two other moduli: the bulk modulus B, which is calculated from the distribution of dilatations $\delta \equiv e_{xx} + e_{yy} + e_{zz}$; and the 'rotated shear modulus' μ'_{shear}, that is, the shear modulus in a coordinate system rotated by 45° around one of the cubic axes (e.g. the lattice Z-axis), calculated from the shear strains $e_{x'y'}$ in the rotated frame. Then

$$c_{11} = B + \frac{4}{3}\mu'_{\text{shear}} \ , \ c_{12} = B - \frac{2}{3}\mu'_{\text{shear}} \tag{2}$$

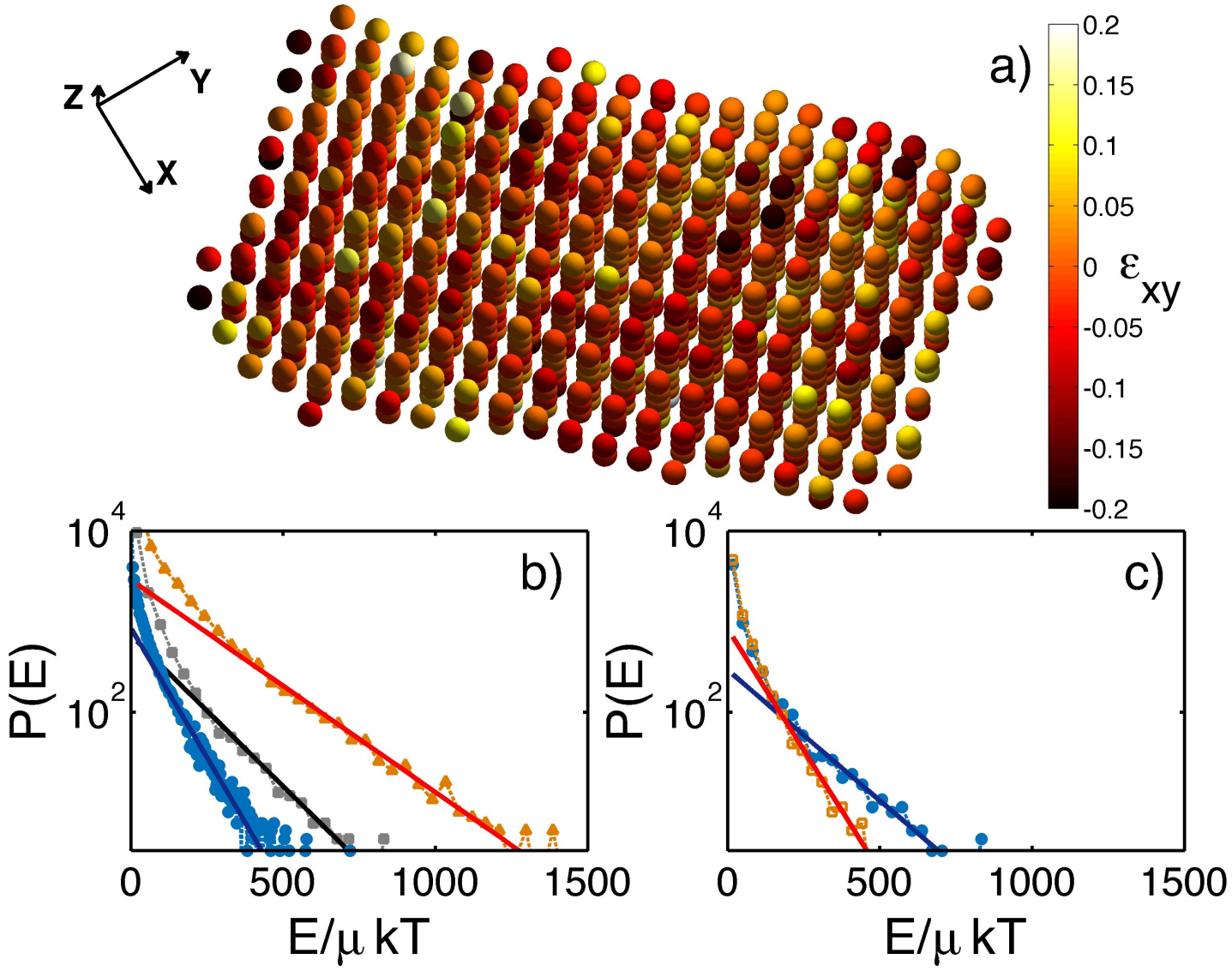

Figure 3: (Color online) a) Local shear strains in a colloidal Wigner crystal. Particles are shown on their lattice positions rather than their true positions, and are color-coded according to the local value of shear strain ε_{xy}. The cubic axes of the crystal are indicated as the X, Y, and Z directions. b) Thermal distribution of strain energies, calculated using an averaging volume $V = (2l)^3 \approx 300(\mu\text{m})^3$. Distributions are shown for energy contributions of the shear strain relative to the cubic axes (blue, lower curve); dilatation (grey/black, middle curve); and shear strain relative to a rotated reference frame (orange/red, upper curve). For both shear strains, the distribution is the sum of the distributions of the three equivalent components. Shown with best-fit lines; the slopes of these lines give the shear modulus c_{44}; the bulk modulus B; and a 'rotated shear modulus' μ'_{shear}, respectively. c) Distribution of strain energies for dilatation, with positive strains (expansion; filled blue circles) and negative strains (compression; open orange squares) distinguished. Shown with best-fit lines, giving approximate bulk modulus for expansion ($B_+ = 6.6$mPa) and for compression ($B_- = 12$mPa). In (b,c), distributions are aggregated over all timesteps. All plots are for number density $n = 0.054(\mu m)^{-3}$.

Example averaged strain energy distributions for the sample at number density $n = 0.054(\mu\text{m})^{-3}$ are shown in Fig. 3b, with the fits giving the elastic moduli $c_{44} = 13\text{mPa}$, $B = 7.7\text{mPa}$, and $\mu'_{\text{shear}} = 5.4\text{mPa}$. Note that the two shear moduli are different, that is, the shear modulus depends on the direction of shear relative to the crystalline axes. Distributions for equivalent shear strain components (e.g. e_{xy}, e_{xz}, and e_{yz}) are summed before fitting. The deviation from the exponential behavior at small values of $E/\mu kT$ is not yet understood, but may be related to the density of states [28].

The crystalline elastic constants vary with number density (Fig. 4a). The relations $c_{12} \lesssim c_{44} < c_{11}$ always hold, and the elastic constants increase with number density as expected. Furthermore, the crystals are strongly anisotropic at all number densities. The anisotropy is quantified by $\Delta \equiv 2c_{44} - (c_{11} - c_{12})$, so that $\Delta = 0$ for an isotropic system. We find $\Delta > 0$ at all number densities (Fig. 4b), with an increase in anisotropy as the number density decreases toward the melting transition.

We also observe the nonlinearity of the stress-strain relationship in the distribution of dilatations. The elastic 'constant' applies only at small strains, where the potential well experienced by a particle due to interparticle interactions is harmonic; at larger strains, the stress-strain relationship may soften or stiffen. The difference between expansion and compression in the dilatations is readily seen, by separating the distributions for positive and for negative strain (Fig. 3c). In the example at number density $n = 0.054(\mu\text{m})^{-3}$, the 'average' elastic constant for expansion is $B_+ = 6.6\text{mPa}$, while the 'average' elastic constant for compression is $B_- = 12\text{mPa}$.

These results are in qualitative agreement with several previous experiments. These experiments were carried out with smaller particles at higher number density; to make order-of-magnitude comparisons, we assume that the elastic moduli vary roughly linearly with number density, that is, that the energy of interaction is of the same magnitude across systems [5]. Using this scaling, we find order-of-magnitude agreement of our c_{11} with Young's modulus measured from the variation of lattice constant with gravitational pressure [5]; of c_{44} with an isotropically averaged shear modulus measured mechanically [7]; and of all three elastic constants with those obtained by measuring dispersion curves using light-scattering [6]. The anisotropy in our crystals is much larger than that found in these latter experiments, presumably due to our larger value of the interparticle spacing relative to the screening length κ^{-1}, quantified by the parameter $\lambda \equiv \kappa n^{-1/3}$; in our experiments, $\lambda \approx$ 5-6, whereas $\Delta/c_{44} \approx 0.14$ at $\lambda \approx 4$ in the previous experiments [6].

Our experimental results do not agree with early lattice dynamics simulations [15], which found much larger anisotropies ($\Delta/c_{44} > 1.7$ for $\lambda \geq 1$); these simulations found the relation $c_{12} \approx c_{11}$ to hold [15], giving the large anisotropy, in contrast to the relation $c_{12} \lesssim c_{44} < c_{11}$ in our experiments. The source of this discrepancy is unknown.

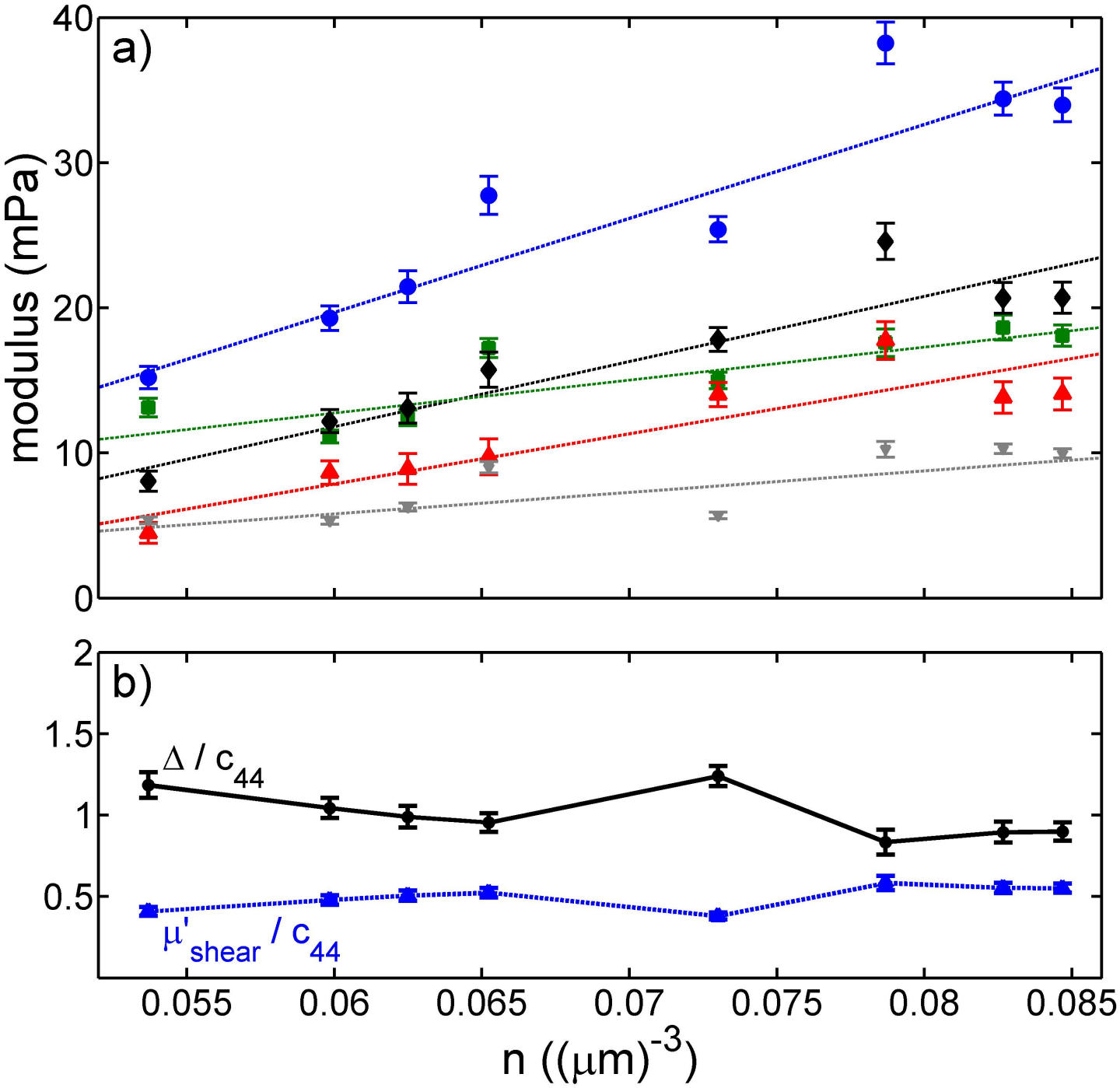

Figure 4: (Color online) a) Variation of elastic constants with number density: tensile modulus c_{11} (blue circles); bulk modulus B (black diamonds); shear modulus c_{44} (green squares); c_{12} (red up-triangles); and rotated shear modulus $\mu'_{\rm shear}$ (grey down-triangles). Error bars give the 95% confidence intervals on the fits. Lines are guides to the eye. b) Variation of elastic anisotropy with number density: Δ/c_{44} (upper curve) and $\mu'_{\rm shear}/c_{44}$ (lower curve) are two complementary measures of the anisotropy. Δ/c_{44} is 0 for an isotropic system, with a maximum possible value of 2 for a shear-stable system; note that these crystal are markedly anisotropic, with $\Delta/c_{44} > 0$ at all number densities accessed.

The experimental results are largely reproduced by simple numerical estimates. We assume a Yukawa interaction

$$U/\text{particle} = U_0 \, \frac{1}{2} \sum_i \frac{\exp\left(-\kappa r_i\right)}{r_i} \tag{3}$$

with the sum taken over neighboring particles, and r_i the interparticle distance; we consider particles on a perfect b.c.c. lattice, taking into account the interactions with 64 nearest neighbors (the first 6 neighbor shells). The value of the screening length, $\kappa^{-1} = 0.45\mu$m, is chosen to reproduce the experimental values of the anisotropy at the same number densities, while the overall energy scaling factor $U_0 = 10^{-23}$Jm $\approx 60(\text{eV} \cdot \mu\text{m})$ is chosen to obtain elastic constants of the same order of magnitude. The resulting numerical estimates for the elastic moduli and anisotropy are shown in Fig. 5.

The values $\kappa^{-1} = 0.45\mu$m and $U_0 = 10^{-23}$Jm are in line with our expectations. Our *a priori* estimate of the screening length κ^{-1} was on the order of ≈ 0.8 - 1μm, based on the added AOT concentration and the results of earlier conductivity measurements in particle-free AOT solutions [16, 17]. We expect the addition of particles to decrease the screening length, as the additional counterions that dissociate from the particle surfaces contribute to the screening; indeed, we expect κ^{-1} to decrease further with increasing number density, which is not accounted for in the simple numerical model. If we estimate an effective particle charge from the interaction strength, we find $Z^* \approx \sqrt{U_0 \epsilon \epsilon_0} \approx 100e$. This is a very rough order of magnitude estimate, but is consistent with the effective charges reported in a number of earlier studies [16, 17, 18].

These numerical estimates reproduce many aspects of our experimental results (Fig. 4). Most notably, the increase in anisotropy with decreasing number density is similar. The elastic constants themselves increase with increasing number density as expected; the slower increase in the experimental results compared to the numerical estimates may be a result of the experimental value of κ^{-1} changing with number density as discussed above. The nonlinearity of the stress-strain relationship is also reproduced: relative to its value at small strains ($\delta \approx 0$), the numerical second derivative of system energy with respect to dilatation, $\partial^2 U/\partial \delta^2 \approx B$, is 24% smaller when evaluated at $\delta = 0.1$ (expansion), and 31% larger when evaluated at $\delta = -0.1$ (compression). The shear stress-strain relationship, in contrast, is quite linear even up to large strains of $e = 0.2$, with the second derivative of energy $\partial^2 U/\partial e^2 \approx c_{44}$ varying by less than 7%. We note, however, that the values of c_{11}, c_{12}, and B given by the numerical estimates are larger relative to c_{44} than are those values calculated from the experimental results. This may be an indication of the presence of many-body effects, which contribute to these bulk elastic constants but not to the shear elastic constant [29]; we discuss this possibility further below. The discrepancy may also be related to the nonlinearity in the bulk elastic constants; while the numerical estimates give c_{11} and B in the small-strain limit, the values obtained experimentally are a less well-defined average of the elastic constants over a range of

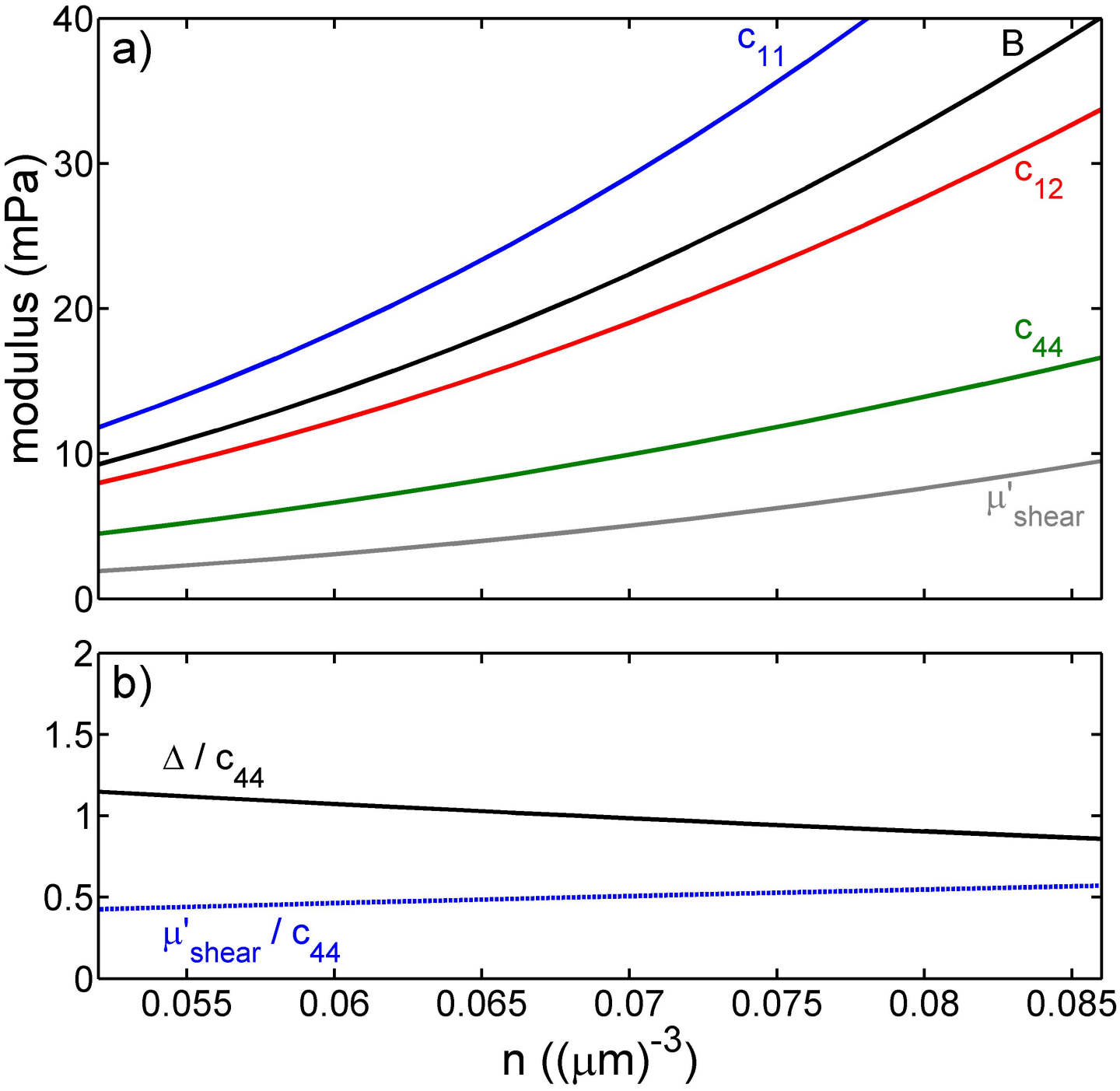

Figure 5: (Color online) Variation with number density of a) elastic constants and b) anisotropy, calculated using a simple numerical model of particles on a perfect b.c.c. lattice interacting via a Yukawa potential. $U_0 = 10^{-23}$Jm, $\kappa^{-1} = 0.45\mu$m. c_{44}, c_{11}, and B are calculated directly; c_{12} and $\mu'_{\rm shear}$ are inferred from c_{11} and B. The range of number densities is chosen to match our experimental results.

strain values encompassing both expansion and compression. Yet for the most part, a very simple model captures the qualitative behavior of the experimental system, and in particular the variation of the anisotropy with number density.

The Cauchy relation predicts that $c_{12} = c_{44}$ for the centrosymmetric b.c.c. lattice with two-body Yukawa interactions [30]. Our experimental results suggest that $c_{12} < c_{44}$ at most number densities, suggesting the possible importance of many-body interactions, though the results are not conclusive. These results are similar to those found in earlier experiments on face-centered-cubic (f.c.c.) crystals of charged colloids, where the violation of the Cauchy relation provided clear evidence that many-body effects are important in charged colloids at high volume fraction [29]. Our possible violation is of a smaller magnitude than that in the f.c.c. crystals, likely because our particle volume fraction is lower. Violation of the Cauchy relation is just one source of evidence for many-body interactions in charged colloid systems: three-body effective forces have been predicted by numerical solutions to the *non*-linearized Poisson-Boltzmann equation [31]; and many-body forces have been measured directly in recent experiments on isolated systems of just a few colloidal particles under experimental conditions similar to ours [32].

Particle fluctuations are not independent, but have a collective nature. This collective behavior is quantified by the correlations of the fluctuations; in particular, we calculate the spatial autocorrelation for each strain component:

$$C_{\epsilon_{ij}}(\mathbf{\Delta r}) \equiv \frac{\left\langle \left(\varepsilon_{ij}(\mathbf{r}) - \langle \varepsilon_{ij} \rangle\right) \cdot \left(\varepsilon_{ij}(\mathbf{r} + \mathbf{\Delta r}) - \langle \varepsilon_{ij} \rangle\right) \right\rangle}{\left\langle \left(\varepsilon_{ij}(\mathbf{r}) - \langle \varepsilon_{ij} \rangle\right)^2 \right\rangle} \tag{4}$$

with the average taken over all reference positions $\mathbf{r}$ and all times t. We restrict the displacements $\mathbf{\Delta r}$ to the lattice vectors, and associate each particle with its nearest lattice position to calculate the correlation; this avoids calculating correlations at non-lattice-vector displacements with very low statistics. Examples of these correlations are shown in Fig. 6. These fields show only short-range correlations of strains in the system, over about 3 lattice spacings. That we do not observe evidence of longer-range vibrational modes is consistent with earlier experiments. Propagating transverse modes have been predicted at long wavelengths [6, 7], while modes with small damping coefficients appear as resonant modes of externally-driven standing shear waves, and are used to measure the shear moduli of colloidal crystals [7, 33]. More recently, the transition from overdamped to propagating transverse modes in aqueous b.c.c. colloidal crystals was observed for the first time [34]; however, such propagating modes are not observable when the sample dimensions are too small [6, 34], as we expect to be the case in our experiments.

Finally, we note that the correlation fields are constant across different number densities. For many examples of strain component and direction, there is little variation or trend with number density. This type of correlation field is characteristic of the Wigner crystals over the range of number densities studied.

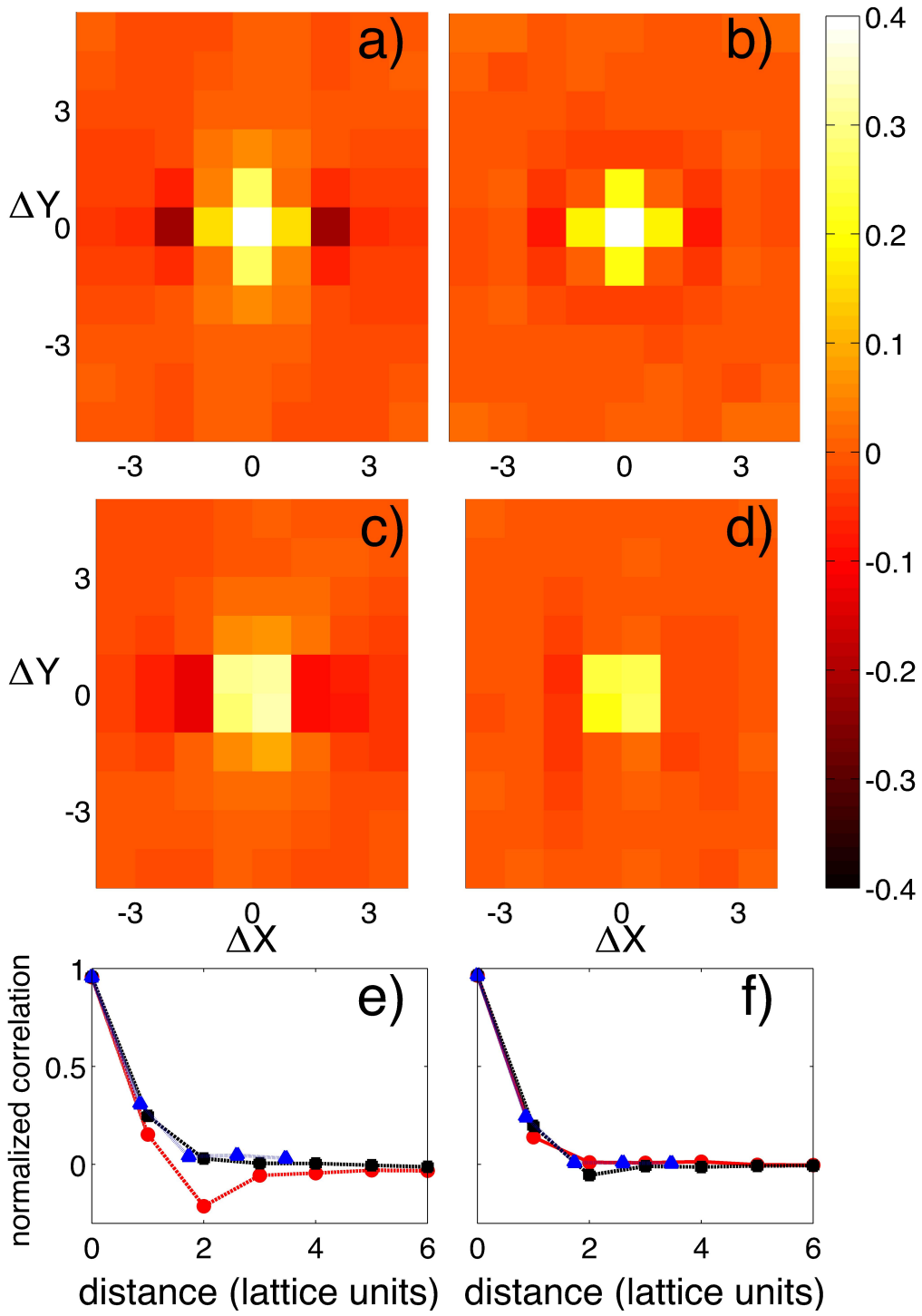

Figure 6: (Color online) Normalized spatial autocorrelations of the strain components in a colloidal Wigner crystal. (a-d) Correlation fields of a) the uniaxial strain ε_{xx}, plotted in the XY plane; b) the shear strain ε_{xy}, plotted in the XY plane; c) the uniaxial strain ε_{xx}, plotted in the nearest-neighbor plane, parallel to, but $1/2$ a lattice constant offset from the plane in (a); d) the shear strain ε_{xy}, plotted in the same nearest-neighbor plane. In (a-d), $\mathbf{\Delta r}$ is restricted to lattice vectors, and particles associated with their nearest lattice position before calculating the correlation. (e-f) One-dimensional cuts of the correlation fields along several directions for e) the uniaxial strain ε_{xx} correlation and f) the shear strain ε_{xy} correlation. Red circles: the cut along the (cubic) X axis (e) and Z axis (f); black squares: the average of the cuts along the other two cubic axes; blue triangles: the average of the cuts along the nearest-neighbor directions. All plots are for number density $n = 0.054(\mu\text{m})^{-3}$; results for other number densities are similar.

4 Conclusion

We have observed that a charged-sphere system of colloidal particles with long-range repulsion forms body-centered-cubic colloidal 'Wigner' crystals at low volume fractions of $\phi \gtrsim 15\%$, in contrast to hard-sphere crystals which form face-centered-cubic structures only at much higher volume fractions. The soft interactions in a colloidal Wigner crystal permit large fluctuations of the particles within the crystal, with typical root-mean-squared displacements up to $\approx 20\%$ of the nearest-neighbor spacing (Lindemann parameter of $\delta_L \approx 0.20$). This parameter is roughly constant over the range of number densities observed. We also measure the thermally-activated local strains in the system as a measure of the fluctuations, and find that in spite of the long-range ordering, the damping fluid restricts correlations in the strains to about two to three lattice spacings; the correlations are also almost uniform with volume fraction.

We measure the crystalline elastic constants c_{11}, c_{12}, and c_{44}, and find them all to be on the order of 10mPa, emphasizing the pronounced softness of these crystals. The crystals remain strongly anisotropic at all number densities, as indicated by the nonzero values of $\Delta \equiv 2c_{44} - (c_{11} - c_{12})$, with the anisotropy increasing with decreasing volume fraction. These results are qualitatively consistent with numerical estimates and with values reported in the literature.

These colloidal Wigner crystals offer the opportunity to study remarkably soft crystals with a structure uncommon in colloidal systems, and to study both the unusually large fluctuations and the material properties of this phase.

5 Acknowledgements

Thanks to Jeroen Appel for synthesizing the PMMA particles, and to Nicholas Schade and Joe McDermott for assistance with system characterization. Joris Sprakel carried out the experiments which initially inspired this further work [18], and we have benefited from conversations with him, with Peter Schall, and with Jan Tobochnik. We also thank Katharine Jensen for the use of her particle tracking and strain calculation codes. This material is based upon work supported by the NSF through the Graduate Research Fellowship (DGE-0946799 and DGE-1144152; E.R.R.), DMR-1310266, DMR-1206765, and the Harvard MRSEC (DMR-0820484).

References

[1] P. N. Pusey and W. van Megen, Nature **320**, 340 (1986).

[2] M. E. Leunissen, C. G. Christova, A.-P. Hynninen, C. P. Royall, A. I. Campbell, A. Imhof, M. Dijkstra, R. van Roij, and A. van Blaaderen, Nature **437**, 235 (2005).

[3] R. Williams and R. Crandall, Phys. Lett. A **48**, 225 (1974).

[4] R. Williams, R. Crandall, and P. Wojtowicz, Phys. Rev. Lett. **37**, 348 (1976).

[5] R. S. Crandall and R. Williams, Science **198**, 293 (1977).

[6] A. J. Hurd, N. A. Clark, R. C. Mockler, and W. J. O'Sullivan, Phys. Rev. A **26**, 2869 (1982).

[7] H. M. Lindsay and P. M. Chaikin, J. Chem. Phys **76**, 3774 (1982).

[8] L. K. Cotter and N. A. Clark, J. Chem. Phys **86**, 6616 (1987).

[9] E. B. Sirota, H. D. Ou-Yang, S. K. Sinha, P. M. Chaikin, J. D. Axe, and Y. Fujii, Phys. Rev. Lett. **62**, 1524 (1989).

[10] C. P. Royall, M. E. Leunissen, and A. van Blaaderen, J. Phys.: Condens. Matter **15**, S3581 (2003).

[11] A. Yethiraj and A. van Blaaderen, Nature **421**, 513 (2003).

[12] M. E. Leunissen and A. van Blaaderen, J. Chem. Phys **128**, 164509 (2008).

[13] E. Wigner, Trans. Faraday Soc. **34**, 678 (1938).

[14] K. Kremer, M. O. Robbins, and G. S. Grest, Phys. Rev. Lett. **57**, 2694 (1986).

[15] M. O. Robbins, K. Kremer, and G. S. Grest, J. Chem. Phys **88**, 3286 (1988).

[16] M. F. Hsu, E. R. Dufresne, and D. A. Weitz, Langmuir **21**, 4881 (2005).

[17] T. Kanai, N. Boon, P. J. Lu, E. Sloutskin, A. B. Schofield, F. Smallenburg, R. van Roij, M. Dijkstra, and D. A. Weitz, (unpublished).

[18] J. Sprakel, P. J. Lu, T. E. Angelini, F. Spaepen, P. Schall, and D. A. Weitz, (unpublished).

[19] J. C. Crocker and D. G. Grier, J. Colloid Interface Sci. **179**, 298 (1996).

[20] Y. Gao and M. L. Kilfoil, Optics Express **17**, 4685 (2009).

[21] Further details on both experiments and analysis are available in E. R. Russell, *Structure and Properties of Charged Colloidal Systems*, PhD thesis, Harvard Unviersity (2014).

[22] The number density is determined geometrically from the lengthscale of the best-fit lattice described later. The volume fraction is obtained from the number density assuming a particle diameter of 1.79μm, measured using dynamic light-scattering on a dilute sample. The uncertainty in this diameter measurement, and in particular the uncertainty in the relation of the measured hydrodynamic diameter to the hard-sphere core diameter, may introduce a systematic error in the reported volume fractions.

[23] F. A. Lindemann, Phys. Z. **11**, 609 (1910).

[24] J. J. Gilvarry, Phys. Rev. **102**, 308 (1956).

[25] M. L. Falk and J. S. Langer, Phys. Rev. E **57**, 7192 (1998).

[26] P. Schall, D. A. Weitz, and F. Spaepen, Science **318**, 1895 (2007).

[27] K. E. Jensen, *Structure and defects of hard-sphere colloidal crystals and glasses*, Ph.D. thesis, Harvard University (2013).

[28] J. Tobochnik, (private communication).

[29] D. Reinke, H. Stark, H.-H. von Grünberg, A. B. Schofield, G. Maret, and U. Gasser, Phys. Rev. Lett. **98**, 038301 (2007).

[30] J. Weiner, *Statistical Mechanics of Elasticity* (Courier Dover Publications, 2002).

[31] C. Russ, H. H. von Grünberg, M. Dijkstra, and R. van Roij, Phys. Rev. E **66**, 011402 (2002).

[32] J. W. Merrill, S. K. Sainis, and E. R. Dufresne, Phys. Rev. Lett. **103**, 138301 (2009).

[33] P. Wette, H. J. Schöpe, and T. Palberg, Colloids and Surfaces A **222**, 311 (2003).

[34] B. V. R. Tata, P. S. Mohanty, M. C. Valsakumar, and J. Yamanaka, Phys. Rev. Lett. **93**, 268303 (2004).